Low-order dynamical model for low-Prandtl number fluid flow in a laterally heated cavity

Cheng-Jun Jing, Daniel Henry,[a] and Hamda Ben Hadid
Laboratoire de Mécanique des Fluides et d'Acoustique—UMR CNRS 5509,
Ecole Centrale de Lyon/Université Claude Bernard–Lyon 1, ECL, BP 163, 69131 Ecully Cedex, France

Nobuyoki Imaishi
Institute of Advanced Material Study, Kyushu University, Kasuga Koen 6-1, Kasugashi 816-8580, Fukuoka, Japan

(Received 13 September 2002; accepted 26 March 2003; published 25 June 2003)

By applying proper orthogonal decomposition (method of snapshots) to low Prandtl number fluid flow in a laterally heated cavity of dimensions $4\times2\times1$ in length×width×height, characteristic basic modes have been extracted. Using Galerkin projection of the governing equations on these basic modes, a low-dimensional dynamical model (set of ordinary differential equations) was constructed. Some results obtained from the low-order model are presented and compared with those calculated by direct numerical simulation (DNS). The factors influencing the reliability of the low-order model such as the length of the reference signal, the snapshot density, the number of modes chosen for Galerkin projection, the characteristic velocity, and the chosen expansions for velocity and temperature are discussed. It is found that the low-order model can exactly reproduce the results obtained by DNS at the design conditions (i.e., for the Grashof and Prandtl numbers at which the basic modes have been obtained). The model can also fairly well approach the DNS results in a domain around these conditions. Nevertheless, it seems that such models have to be used with care and that, in any case, they can qualitatively predict the DNS results only in a not very large range around the design conditions. © *2003 American Institute of Physics.*
[DOI: 10.1063/1.1577119]

I. INTRODUCTION

Since the initial work of Lumley,[1] proper orthogonal decomposition (POD) has been widely applied to analysis of flows (see, for example, in Ref. 2). Especially after Sirovich[3] proposed a so-called method of snapshots, the use of POD for the construction of low-order models [systems of ordinary differential equations (ODEs)] for complicated flows becomes feasible. As it is well known, in order to understand the behavior of complicated flows, direct numerical simulation (DNS) of the partial differential equations (PDEs) governing the flow is commonly used. Three-dimensional (3D) DNS usually consumes much time and computation fees. In contrast, solution of ODEs is far less consuming. In addition, by solving ODEs, it is easy to reveal the global behavior of the system (i.e., to establish bifurcation diagrams) with respect to control parameters such as Reynolds, Grashof, or Prandtl numbers. Therefore, many efforts have been made in order to construct reliable low-order models. However, most of the studies concern either forced flows (apart from studies about the transition to turbulence, see Refs. 4–8) or thermal effects,[9] i.e., problems without coupling of temperature and velocity. Besides, these studies were mostly applied to two-dimensional problems. For thermal convection problems, although Sirovich[3,10] described an approach for the construction of the ODE systems which treats velocity and temperature together regardless of their different properties, reports based on low-order model analysis are still few. Recently, Gunes and co-workers[11–13] presented some results concerning the application of POD to two-dimensional (2D) heated situations and obtained by treating separately velocity and temperature; however, they did not analyze the advantages of this treatment and the reliability of the constructed ODE system. Podvin and Le Quéré[14] applied POD to obtain low-order models for the flow in a differentially heated cavity (tall 2D cavity). They wanted to determine how well very low dimensional models can reproduce the flow obtained by DNS. They used an approach which treats velocity and temperature together, but with a rescaling factor as was suggested by Lumley and Poje.[15] The purpose of this paper is to discuss how to construct a reliable low-order model for 3D thermal convection problems by applying POD and the method of snapshots.

II. PROBLEM FORMULATION AND SIMULATION METHOD

Thermal convection in low-Prandtl number fluids in a laterally heated rigid cavity (Fig. 1) was chosen as the purpose of this paper since this subject is of interest for many material processing situations (problem of the transition to unsteadiness) and has been widely studied only in two-dimensional cases.[16,17] Few three-dimensional results have

[a]Author to whom correspondence should be addressed. Electronic mail: henry@mecaflu.ec-lyon.fr

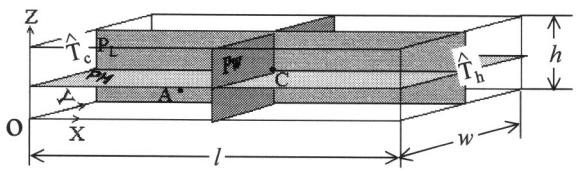

FIG. 1. Laterally heated cavity with dimensions $4\times2\times1$, respectively, in length (along X), width (along Y), and height (along Z). P_L, P_W, and P_H: The three principal planes. C: The center point. A (1,1,0.25): The monitoring point for time variation of velocity and temperature.

been obtained (see in Henry and Buffat[18] and Ref. 19) whereas some experimental results are available (see in Roux[16] and Refs. 19 and 20).

The cavity considered in this study is parallelepipedic with dimensions l (length), w (width) and h (height). The main planes in the cavity are shown in Fig. 1, the P_L plane (vertical longitudinal middle plane), the P_W plane (vertical transverse middle plane), and the P_H plane (horizontal middle plane). The right hand sidewall of the cavity is kept at a constant temperature $\hat{T}_h$ and the left hand sidewall at a constant lower temperature $\hat{T}_c$, which gives a temperature difference $\Delta T=\hat{T}_h-\hat{T}_c$. The other four walls are adiabatic. No-slip boundary conditions are imposed at all boundaries. The fluid is assumed to be an incompressible Newtonian fluid satisfying the Boussinesq approximation. The flow is considered as laminar and the viscous dissipation is negligible. The partial differential equations (PDEs) governing the fluid flow can then be expressed in nondimensional form as

$$\nabla\cdot\boldsymbol{V}=0, \tag{1}$$

$$\frac{\partial\boldsymbol{V}}{\partial\tau}+Gr^{0.5}\boldsymbol{V}\cdot\nabla\boldsymbol{V}=-\nabla P+\nabla^2\boldsymbol{V}+Gr^{0.5}Te_z, \tag{2}$$

$$\frac{\partial T}{\partial\tau}+Gr^{0.5}\boldsymbol{V}\cdot\nabla T=Pr^{-1}\nabla^2T, \tag{3}$$

where $\boldsymbol{V}$ is the fluid velocity vector, T is the temperature, P is the pressure, τ is the time and $\boldsymbol{e}_Z$ is the unit vector along Z-direction. The nondimensional parameters involved are defined, respectively, as Grashof number $Gr=g\beta\Delta Th^3/\nu^2A_x$, Prandtl number $Pr=\nu/\alpha$, and aspect ratios $A_x=l/h$ and $A_y=w/h$, where g is the acceleration due to gravity, β is the thermal expansion coefficient of the fluid, ν is the kinematic viscosity, and α is the thermal diffusivity. The characteristic scales used for nondimensionalization are h, $Gr^{0.5}\nu/h$, $\rho Gr^{0.5}\nu^2/h^2$ and h^2/ν for length, velocity, pressure and time, respectively, and the dimensionless temperature is defined as $T=(\hat{T}-\hat{T}_c)/(\Delta T/A_x)$. The boundary conditions are:

$U=V=W=0$ on all the boundaries (rigid walls),
$T=0$ at $X=0$ (cold vertical wall),
$T=A_x$ at $X=A_x$ (hot vertical wall),
$\partial T/\partial n=0$ (adiabatic condition) on the horizontal and vertical longitudinal walls, where $\boldsymbol{n}$ indicates the normal direction of walls.

The situation studied in this paper corresponds to a cavity with dimensions $4\times2\times1$ ($A_x\times A_y\times1$). The construction of a low-dimensional dynamical model will be done through the projection of the governing equations on characteristic modes obtained by POD. To get these POD modes, three-dimensional direct numerical simulations are required. They will be performed by using a code already developed for crystal growth applications[21] and based on the finite difference method. The convective terms were discretized by a modified Kawamura scheme of third-order accuracy[22] and the diffusive terms were discretized by the conventional center difference of second-order accuracy. The time derivative term was explicitly approximated by a first-order forward difference. The velocity and pressure expressed on a staggered grid were modified simultaneously by the highly simplified marker-and-cell algorithm.[23] Tests of precision were realized on different grids, $70\times28\times22$, $80\times34\times26$, $90\times40\times30$, and $100\times46\times34$ for typical values of the parameters, $Gr=45\,000$ and $Pr=0.015$. Except for the case with the coarse grid, $70\times28\times22$, the results obtained on the grids $80\times34\times26$, $90\times40\times30$, and $100\times46\times34$ were oscillatory and similar. The maximum velocities obtained on the grids $80\times34\times26$ and $90\times40\times30$ are only 1.21% and 0.87%, respectively, larger than that obtained on the finest grid $100\times46\times34$. Therefore, the grid $90\times40\times30$ was chosen to simulate the oscillatory flow in the cavity under the consideration of both the accuracy and the computational time. At last, the nondimensional time step was set to $\Delta\tau=5\times10^{-7}$, a value which was verified to meet both numerical stability condition and Courant condition.

III. PROPER ORTHOGONAL DECOMPOSITION (POD)

POD is a rigorous procedure for extracting a basis of characteristic modes from sampled time evolution signals. These modes are the eigenfunctions of an integral operator based on the spatial correlation function. They are shown to form an orthogonal basis for the function space in which the process resides, and to represent this process in the most efficient way.[9,10] Directly applying this procedure to a 3D discretized problem involves extremely considerable computing task because the spatial correlation matrix (the eigenvalues of which we want to obtain) is usually very large. For the case under consideration in our study, the matrix would have a dimension of $90\times40\times30$ which corresponds to the number of grid points. A more accessible approach which is referred to as the method of snapshots was proposed by Sirovich.[3] This method which invokes the ergodic hypothesis allows to reduce the computation task to a much more tractable eigenproblem with a size N equal to the number of snapshots of the flow field which have been obtained by direct numerical simulation (usually of the order of some hundreds). The method of snapshots which is applied to our problem is presented in a practical way in the following.

The state variables $\boldsymbol{V}(\boldsymbol{x},\tau)$ and $T(\boldsymbol{x},\tau)$ obtained through the N snapshots are decomposed into time-averaged parts, $\overline{\boldsymbol{V}}(x)$ and $\overline{T}(\boldsymbol{x})$, and time-varying parts, $\boldsymbol{v}'(\boldsymbol{x},\tau)$ and $T'(\boldsymbol{x},\tau)$, i.e.,

$$\boldsymbol{V}(\boldsymbol{x},\tau)=\overline{\boldsymbol{V}}(\boldsymbol{x})+\boldsymbol{v}'(\boldsymbol{x},\tau), \tag{4}$$

$$T(\boldsymbol{x},\tau)=\overline{T}(\boldsymbol{x})+T'(\boldsymbol{x},\tau). \tag{5}$$

The two time correlation matrices $C^V_{m,n}$ and $C^T_{m,n}$ are then constructed from the velocity and temperature samples, respectively, as

$$C^V_{m,n}=\frac{1}{N}(\boldsymbol{v}'(\boldsymbol{x},\tau_m),\boldsymbol{v}'(\boldsymbol{x},\tau_n)),\quad m,n=1,2,...,N, \tag{6}$$

$$C^T_{m,n}=\frac{1}{N}(T'(\boldsymbol{x},\tau_m),T'(\boldsymbol{x},\tau_n)),\quad m,n=1,2,...,N, \tag{7}$$

where the outer parentheses (.,.) represent the inner product defined as

$$(\boldsymbol{a},\boldsymbol{b})=\int_D \boldsymbol{a}(\boldsymbol{x})\cdot\boldsymbol{b}(\boldsymbol{x})d\boldsymbol{x}, \tag{8}$$

where $\boldsymbol{a}$ and $\boldsymbol{b}$ are two vectors for Eq. (6) and two scalars for Eq. (7) and D is the flow domain.

The eigenvalues λ^V_i and λ^T_i associated to these matrices, and their corresponding eigenvectors A^m_i and B^m_i, $m=1,N$, can be calculated, which gives

$$C^V_{m,n}A^n_i=\lambda^V_i A^m_i \tag{9}$$

and

$$C^T_{m,n}B^n_i=\lambda^T_i B^m_i. \tag{10}$$

Finally, the characteristic modes (also called empirical eigenfunctions) $\boldsymbol{\Phi}_i(\boldsymbol{x})$ and $\Theta_i(\boldsymbol{x})$ (here normalized) are obtained as linear combinations of the time-varying parts

$$\boldsymbol{\Phi}_i(\boldsymbol{x})=\sum_{m=1}^{N} A'^m_i\boldsymbol{v}'(\boldsymbol{x},\tau_m) \tag{11}$$

and

$$\Theta_i(\boldsymbol{x})=\sum_{m=1}^{N} B'^m_i T'(\boldsymbol{x},\tau_m), \tag{12}$$

with

$$A'^m_i=A^m_i\Big/\sqrt{\lambda^V_i N\sum_{m=1}^{N}(A^m_i)^2}$$

and

$$B'^m_i=B^m_i\Big/\sqrt{\lambda^T_i N\sum_{m=1}^{N}(B^m_i)^2}.$$

The method chosen here is based on the separate treatment of velocity and temperature with the construction of a two time correlation matrix for each field, as is also done in Refs. 11–13. Another possibility suggested in other papers[3,10,14,15] would have been to treat velocity and temperature together and define a single two time correlation matrix which could be expressed as

$$C_{m,n}=C^V_{m,n}+\alpha C^T_{m,n}, \tag{13}$$

where α is a rescaling factor, sometimes taken as 1.[3,10]

We will discuss the advantages of the procedure used in this paper in Sec. VI E.

The eigenvalues and empirical eigenfunctions have interesting properties.

(i) The eigenvalues are real, non-negative and can be ordered. Each eigenvalue λ^V_i (or λ^T_i) represents the relative contribution of the corresponding modes $\boldsymbol{\Phi}_i(\boldsymbol{x})$ (or $\boldsymbol{\Theta}_i(\boldsymbol{x})$) to the total fluctuation kinetic energy (or thermal energy).

(ii) The eigenfunctions are orthogonal and have been normalized, so that they verify $(\boldsymbol{\Phi}_i,\boldsymbol{\Phi}_j)=\delta_{i,j}$ and $(\Theta_i,\Theta_j)=\delta_{i,j}$. The velocity eigenfunctions are divergence-free ($\nabla\cdot\boldsymbol{\Phi}_i=0$) since they are constructed as linear combinations of the incompressible flow snapshots $\boldsymbol{v}'$. At last, from Eqs. (4) and (11), and Eqs. (5) and (12), it is easy to understand that the eigenfunctions automatically satisfy the homogeneous boundary conditions associated to the perturbations for the problem under consideration.

In addition, the eigenfunctions found by POD are shown to be optimal for modeling or reconstructing a signal compared to all other decompositions.[5] The time-varying parts $\boldsymbol{v}'(\boldsymbol{x},\tau)$ and $T'(\boldsymbol{x},\tau)$ can then be expressed in terms of these normalized eigenfunctions as

$$\boldsymbol{v}'(\boldsymbol{x},\tau)=\sum_{i=1}^{M_V} a_i(\tau)\boldsymbol{\Phi}_i(\boldsymbol{x}), \tag{14}$$

$$T'(\boldsymbol{x},\tau)=\sum_{i=1}^{M_T} b_i(\tau)\Theta_i(\boldsymbol{x}), \tag{15}$$

where $a_i(\tau)$ and $b_i(\tau)$ are coefficients depending on time, and M_V and M_T are the numbers of the first most important modes retained in the expansion for velocity and temperature, respectively. When $M_V=M_T=N$, the original sampled signal can be reproduced exactly, with

$$a_i(\tau)=a^m_i=N\lambda^V_i A'^m_i \quad\text{and}\quad b_i(\tau)=b^m_i=N\lambda^T_i B'^m_i. \tag{16}$$

Usually M_V and M_T are much smaller than the number of snapshots, N. They are chosen so that the set of eigenfunctions captures most of the fluctuation energy. For example, in Sirovich,[3] the choice is made by taking $\xi>99\%$, where $\xi\equiv\Sigma_{i=1}^{M_V}\lambda^V_i/\Sigma_{i=1}^{N}\lambda^V_i$ or $\Sigma_{i=1}^{M_T}\lambda^T_i/\Sigma_{i=1}^{N}\lambda^T_i$, meaning that the first M_V (M_T) modes capture more than 99% of the fluctuation kinetic energy (thermal energy). The use of these modes to construct a low dimensional model is presented in the next section.

IV. CONSTRUCTION OF LOW-ORDER MODELS

The Galerkin projection of Eq. (2) onto the first M_V basisfunctions $\boldsymbol{\Phi}_i$, and of Eq. (3) onto the first M_T basisfunctions Θ_i can be written as

$$\left(\boldsymbol{\Phi}_i,\frac{\partial V}{\partial\tau}+Gr^{0.5}(\boldsymbol{V}\cdot\nabla\boldsymbol{V}-T\boldsymbol{e}_Z)+\nabla P-\nabla^2\boldsymbol{V}\right)=0,\quad i=1,M_V, \tag{17}$$

$$\left(\Theta_i,\frac{\partial T}{\partial\tau}+Gr^{0.5}\boldsymbol{V}\cdot\nabla T-Pr^{-1}\nabla^2 T\right)=0,\quad i=1,M_T. \tag{18}$$

By substituting Eqs. (4), (5), (14), and (15) into the above equations, and using the relation $(\boldsymbol{\Phi}_i,\nabla P)=\int_\Gamma P(\boldsymbol{n}\cdot\boldsymbol{\Phi}_i)d\Gamma-\int_\Omega P(\nabla\cdot\boldsymbol{\Phi}_i)d\Omega=0$ and the orthonormality of Φ_i and Θ_i, we obtain the following low dimensional dynamical system (nonlinear ODEs) concerning the expansion coefficients a_i and b_l

$$\frac{da_i}{dt} = -Gr^{0.5}(A_{i,j,k}a_j a_k + B_{i,j}a_j - C_{i,m}b_m + D_i) + E_{i,j}a_j + F_i, \tag{19}$$

$$\frac{db_l}{dt} = -Gr^{0.5}(G_{l,j,m}a_j b_m + H_{l,m}b_m + I_{l,j}a_j + J_l) + Pr^{-1}(K_{l,m}b_m + L_l), \tag{20}$$

where $i,j,k=1,M_V$ and $l,m=1,M_T$. The capital letters from A to L are coefficients related to inner products concerning the eigenfunctions and the mean velocity or temperature fields. They are listed in the Appendix. Identical indexes in products indicate summations. In computing these coefficients, the convective terms such as $\mathbf{\Phi}\cdot\nabla\mathbf{\Phi}$ were approximated by the third-order Kawamura scheme[22] and the diffusive terms such as $\nabla^2\mathbf{\Phi}$ by the conventional second-order differentiation, as was done in the DNS code. The integration was approximated by multiplying each nodal estimation by the control volume of the cell. For example, the coefficients $E_{i,j}$ can be expressed as $E_{i,j}=(\mathbf{\Phi}_i,\nabla^2\mathbf{\Phi}_j)=\sum_{m,n=1}^{3}\mathbf{\Phi}_i^m(\partial/\partial x_n)(\partial\mathbf{\Phi}_j^m/\partial x_n)\Delta V$, where $\Delta V=dx_1dx_2dx_3$ is the control volume, $(\Phi^1,\Phi^2,\Phi^3)=(\Phi^u,\Phi^v,\Phi^w)$ are the components of $\mathbf{\Phi}$ and $(x_1,x_2,x_3)=(x,y,z)$ are the coordinates. The free divergence of the flow and the boundary conditions are automatically verified from the properties of the eigenfunctions. This set of nonlinear ODEs has order M_V+M_T, usually of some dozens. It is integrated numerically using either a classical solver or the software AUTO[24] which allows a better analysis of the dynamical behavior with the calculation of bifurcation diagrams.

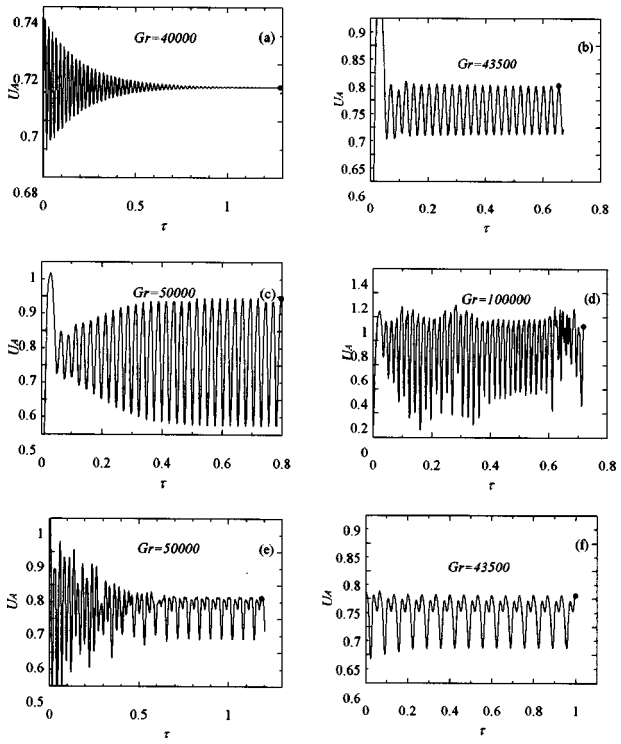

FIG. 2. Time evolution of X-velocity at monitoring point A, U_A, for $Gr=40\,000$, (a); $Gr=43\,500$, (b) and (f); $Gr=50\,000$, (c) and (e), and $Gr=10^5$, (d), in the case of $Pr=0.015$. The DNS initial values used for (a)–(d) are $U=V=W=P=0$ and $T=X$; for (e) ($Gr=50\,000$) it is the DNS result at (d) ($Gr=10^5$) and for (f) ($Gr=43\,500$) it is the DNS result at (e) ($Gr=50\,000$).

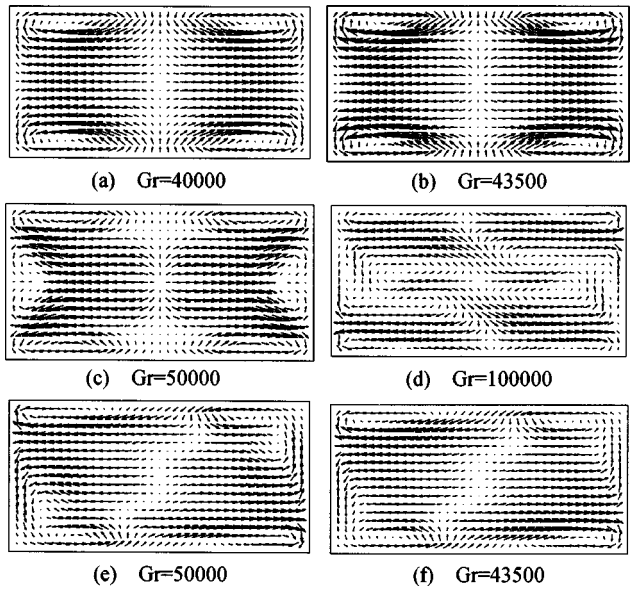

FIG. 3. DNS velocity vectors in P_H plane corresponding to the snapshots marked by (·) in Fig. 2, for $Gr=40\,000$, (a); $Gr=43\,500$, (b) and (f); $Gr=50\,000$, (c) and (e), and $Gr=10^5$, (d), in the case of $Pr=0.015$.

V. RESULTS

A. DNS results

Some 3D DNS have been performed to study thermal convection in low-Pr number fluids in a confined cavity (dimensions of $4\times2\times1$) by using the numerical method presented in Sec. II. We present here some of the results related to the purpose of this paper, for $Pr=0.015$.

Figure 2 shows the time evolutions of the X-velocity at the monitoring point A (see its position in Fig. 1), U_A, for several representative Grashof numbers and Fig. 3 shows the corresponding velocity vectors in P_H plane. When $Gr<Gr_{c1}=43\,250$ (with maximum error of $\pm0.3\%$), the flow

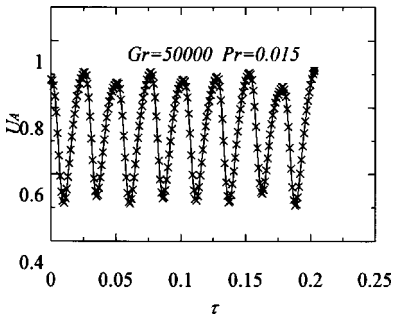

FIG. 4. Time evolution of X-velocity at monitoring point A, U_A, for the signal sample used for proper orthogonal decomposition and construction of low-order model. Snapshots, indicated by (×), are evenly spaced by a time interval equal to 2000 $\Delta\tau$. The sample is collected during the transition from a state with S_L and S_A symmetries to a state with only S_C symmetry, obtained by adding a quite large random perturbation to the flow with S_L and S_A symmetries.

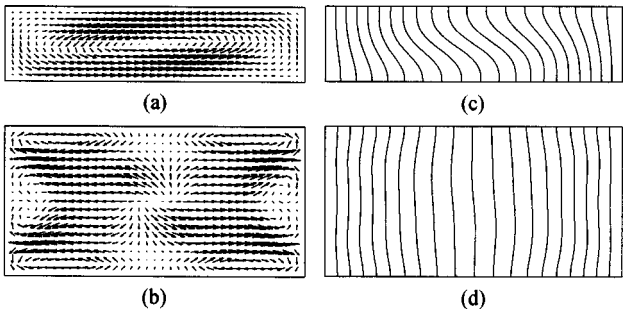

FIG. 5. Snapshots of the velocity vectors of the signal sample in P_L and P_H planes, (a) and (b), and isotherms in P_L and P_H planes, (c) and (d). The corresponding instant is indicated by (·) in Fig. 4.

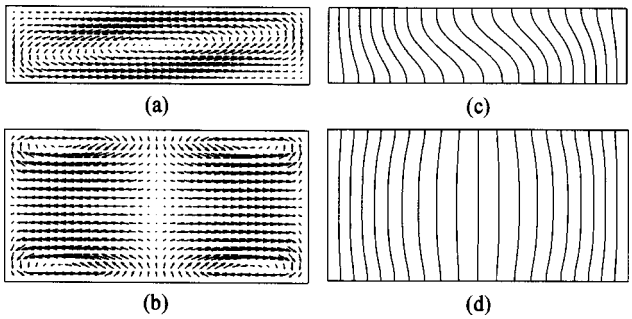

FIG. 6. Velocity vectors in P_L and P_H planes, (a) and (b), and isotherms in P_L and P_H planes, (c) and (d), for the mean flow of the signal sample.

is steady if the DNS is started from motionless state or from flows obtained at smaller Gr [see Fig. 2(a) for $Gr=40\,000$]. This steady flow is symmetric with respect to the plane P_L (S_L symmetry), and to the horizontal axis at the intersection of the planes P_W and P_H (S_A symmetry) [see Fig. 3(a) showing the velocity vectors in plane P_H for $Gr=40\,000$]. Combination of these two symmetries gives also a symmetry S_C with respect to the central point C of the cavity. These symmetries are identical to those obtained by Henry and Buffat.[18] At $Gr=Gr_{c1}$, the steady flow is found to become unstable and to transit to oscillation. With the increase of Gr, the flow first evolves regularly, still corresponding to periodic state with the S_L and S_A symmetries [see Figs. 2(b) and 2(c) for the time evolution of U_A and Figs. 3(b) and 3(c) for the velocity vectors in plane P_H for $Gr=43\,500$ and $Gr=50\,000$, respectively], and then becomes more chaotic, corresponding to a state with only the S_C symmetry [see Fig. 2(d) for the time evolution of U_A and Fig. 3(d) for the velocity vector in plane P_H for $Gr=10^5$]. An interesting point is that if Gr is decreased, starting the DNS with the flow and temperature fields with S_C symmetry obtained at, for example, $Gr=10^5$, the oscillatory flow with S_C symmetry is found down to $Gr=Gr_{LP}=39\,000$ [see Figs. 2(e) and 2(f) for the time evolution of U_A and Figs. 3(e) and 3(f) for the velocity vectors in plane P_H for $Gr=50\,000$ and $Gr=43\,500$, respectively]. This indicates a hysteresis in the range of $Gr>Gr_{LP}$, the flow for $Gr<Gr_{LP}$ being steady independently of the initial conditions (such hysteresis phenomenon in low-Pr number fluid has already been observed experimentally[20] and theoretically).[25,26] This also indicates that the periodic state with S_L and S_A symmetries corresponds to a branch supercritically initiated at Gr_{c1} and the periodic state with only S_C symmetry to a branch subcritically initiated at some Gr slightly higher than Gr_{c1}.

Obtaining more details on the bifurcation diagram in such 3D configuration is a difficult task which is even beyond our present possibilities. For example, for the subcritical branch with S_c symmetry, it would need the direct calculation of Hopf bifurcation points for the determination of the critical Grashof at which the branch is initiated, and also the calculation of unstable periodic states to follow this subcritical branch. On the other hand, such calculations are possible for low-dimensional systems of ODE, and it is why the purpose of the present work is to investigate the ability of the low-order model constructed by the POD method to represent the real flow behavior. The comparisons between DNS results and low-order model will not be exhaustive because of the present limitations of DNS for large systems, but they will be done on important aspects of the real flow, i.e., principally, the critical Grashof number for transition to periodic flow, the frequencies, the symmetries, the hysteresis phenomenon.

B. Sample for POD

To perform POD, a signal sample is needed. We decided to collect a sample from the DNS results for the case of $Gr=50\,000$ and $Pr=0.015$. This case is called the reference

TABLE I. Normalized eigenvalues of some of the most energetic modes and their cumulative contribution to the fluctuation energy at the design conditions $Gr^0=50\,000$ and $Pr^0=0.015$ ($M=204$).

	λ_i^V		λ_i^T	
Index of the mode	Eigenvalue	Cumulative energy contribution (%)	Eigenvalue	Cumulative energy contribution (%)
1	0.5735	57.351	0.6362	63.623
2	0.3652	93.874	0.2043	84.056
3	1.744×10^{-2}	95.618	0.1453	98.584
4	1.615×10^{-2}	97.233	8.294×10^{-3}	99.413
10	4.593×10^{-4}	99.888	3.361×10^{-5}	99.993
15	4.475×10^{-5}	99.982	5.942×10^{-6}	99.999
20	1.149×10^{-5}	99.996	4.426×10^{-7}	>99.999
30	3.761×10^{-6}	99.998	1.953×10^{-7}	>99.999

or design case and will be indicated by a superscript 0, as Gr^0. For this case, from DNS, we have shown that there exist two different periodically oscillatory flows, one with S_L and S_A symmetries and the other with only S_C symmetry. Preparatory studies have shown that if we collect a sample only from the flow with S_L and S_A symmetries, the constructed ODEs can only predict the flow with S_L and S_A symmetries, i.e., cannot predict the flow with S_C symmetry; similarly, ODEs constructed with a sample only collected from the flow with S_C symmetry will miss the flow with S_L and S_A symmetries. A sample combining the flow with S_L and S_A symmetries and the flow with S_C symmetry also did not produce a reasonable prediction. DNS has already indicated that the stable periodic flow with S_C symmetry [Figs. 2(e) and 3(e)] can also be obtained by adding a quite large perturbation to the stable periodic flow with S_L and S_A symmetries [Figs. 2(c) and 3(c)]. The sample used for POD in this paper was then collected during the transition from the periodic oscillation with S_L and S_A symmetries to the periodic oscillation with S_C symmetry by adding a perturbation $\varphi' = \varphi_0 \times (1-2r)$ to φ_0, where φ stands for U,V,W,P,T,r is a random value between 0 and 1, and subscript 0 indicates a snapshot of the stable periodic flow with S_L and S_A symmetries. The time evolution of U_A for the sample is shown in Fig. 4, indicating that the sample obtained is quasi-periodic. The sample covers about eight quasi-periods and consists of $N=204$ snapshots indicated by $(\times)$. The corresponding time interval between two successive snapshots is 2000 $\Delta\tau$.

The flow and temperature fields for the snapshot corresponding to the dot $(\cdot)$ in Fig. 4 are shown in Fig. 5. Only the S_C symmetry is well verified. The flow and temperature fields for the mean flow of the sample are shown in Fig. 6. For the mean flow, S_L and S_A symmetries are well verified together with S_C symmetry.

C. Eigenfunctions obtained by POD

The spatial eigenfunctions (or modes) have been determined by applying the method of snapshots to the above sample.

Some of the largest normalized eigenvalues of matrices (6) and (7) derived from the sample are listed in Table I. The first mode (for velocity as well as for temperature) captures about 60% of the fluctuation energy, whereas the first four modes are enough to capture the main part of the fluctuation energy (more than 97%). These first four modes of velocity and temperature obtained by POD are shown in Fig. 7 by views in P_L and P_H planes. The first two velocity modes clearly have S_L and S_A symmetries together with S_C symmetry, whereas the third and fourth modes only have S_C symmetry. Concerning temperature, in addition to the S_C symmetry, the first and third modes are almost symmetric with regard to S_L and S_A whereas the second and fourth modes are rather antisymmetric.

According to the POD theory, the basis functions obtained at the design conditions form an orthogonal and complete set and are expected to be relevant for cases other than the design case. This implies that the basis functions associated to these new cases might be connected to those obtained

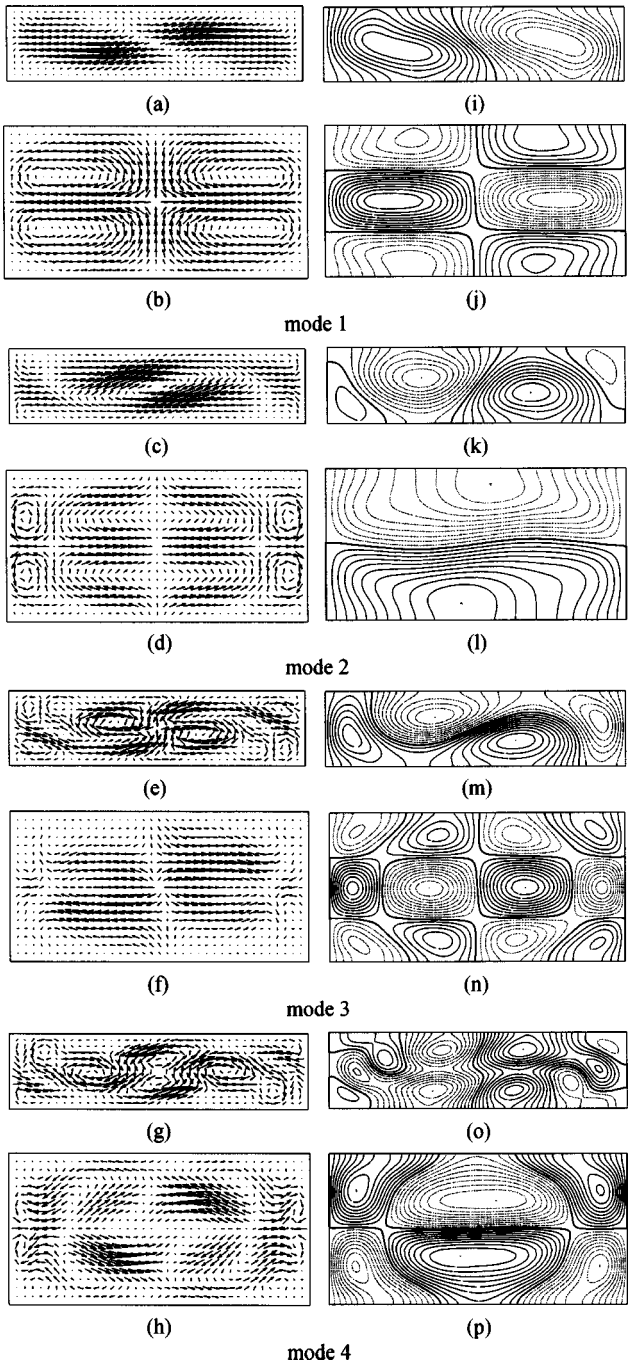

FIG. 7. Velocity vectors in P_L and P_H planes for the first four velocity modes, (a)–(h), and isotherms in P_L and P_H planes for the first four temperature modes, (i)–(p).

at the design case. To check this in our case, the first four most energetic velocity basis functions obtained by POD from the DNS data with S_L symmetry at $Gr=43\,500$ are shown in Fig. 8. The comparison between the basis functions given in Figs. 7 and 8 is rather good, and it can then be expected that the basis functions obtained at the design conditions will be relevant to represent the periodic states with S_L symmetry at Gr values different from Gr^0.

The temporal expansion coefficients obtained by direct projection of the sample data on the computed eigenfunc-

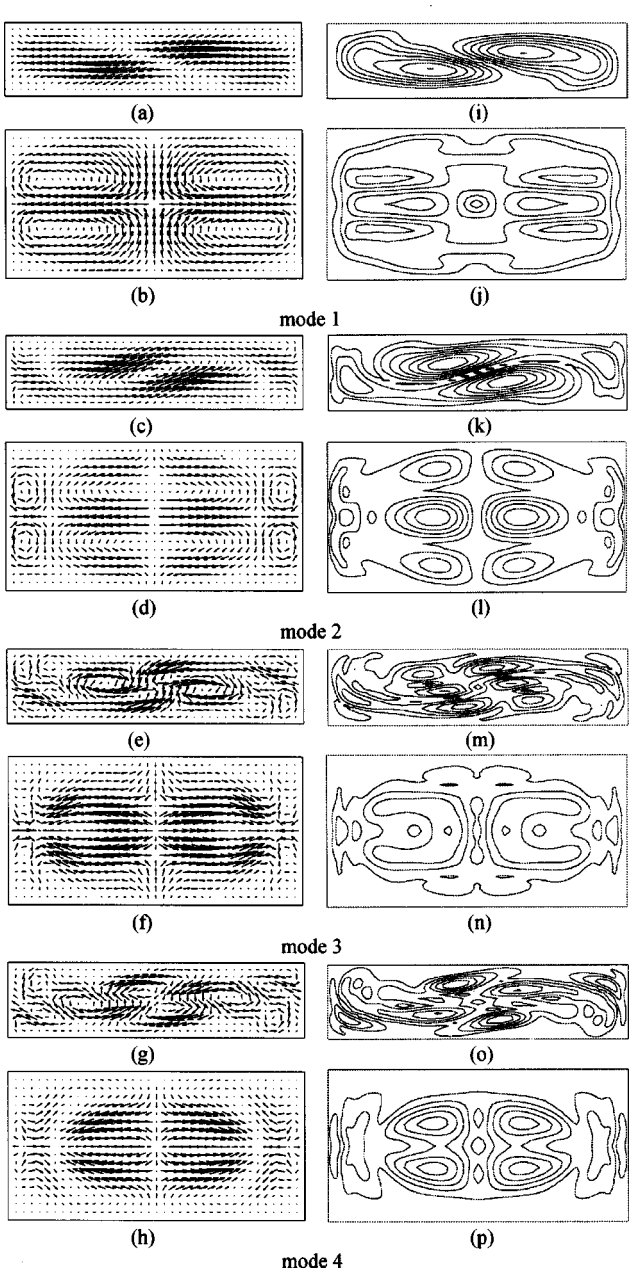

FIG. 8. Velocity vectors, (a)–(h), and contours of speeds, (i)–(p), in P_L and P_H planes for the first four velocity modes for $Gr=43\,500$. These modes were obtained from DNS data with S_L symmetry. The interval between the contours of speeds is 0.2.

tions (denoted reference coefficients or reference results in the following) have been calculated [Eq. (16)]. The first four coefficients for velocity and temperature are given in Fig. 9 as a function of time. The similarities observed in these time evolutions correspond to the similarities observed in the symmetries of the modes. Indeed, the first two velocity modes evolve with the same basic frequency, whereas the third and fourth modes have a frequency which is twice larger. Concerning temperature, it is the first and third modes which evolve with the basic frequency, whereas the second and fourth modes rather have a frequency which is twice smaller.

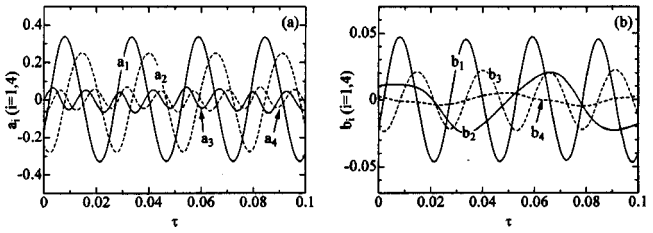

FIG. 9. Time evolution of the first four temporal expansion coefficients for velocity (a) and temperature (b) at the design conditions.

D. Low order model: Results at design conditions

We used the first $M_V=16$ modes of velocity and the first $M_T=10$ modes of temperature, which capture 99.99% of fluctuation kinetic and thermal energy, to construct a low-order model by Galerkin projection [Eqs. (19)–(20)]. The first calculations with this model concern time evolutions at the design parameter values Gr^0 and Pr^0. Starting with the values of the reference coefficients corresponding to the beginning of the sample, the time evolution of the expansion coefficients has been obtained. The results compare very well with what is obtained for the reference coefficients. For example, for the first four coefficients calculated for velocity and temperature, the evolution is indistinct from what is shown in Fig. 9. Moreover, the time evolutions of the reconstructed velocity component U_A and temperature T_A at monitoring point A are plotted in Fig. 10 (dashed lines) and compared with the DNS reference results (solid lines). The evolutions on the sample length (τ roughly from 0 to 0.2) are indistinct, showing that the low-order model works very well locally, i.e., at design conditions. We have to mention that an important requirement in the construction of the low-order model is to use the same spatial discretization of the different terms of the equations as that used in the DNS code.

E. Low-order model: Predicted results with S_L and S_A symmetries

Some calculations were done to check how the low-order model works for values of Gr different from the reference value Gr^0. For $Gr=43\,500$, the low-order model gives a solution which compares well with the DNS solution with S_L and S_A symmetries. Figure 11 shows the time evolution of the predicted velocity and temperature at monitoring point A, together with the corresponding DNS results. The DNS be-

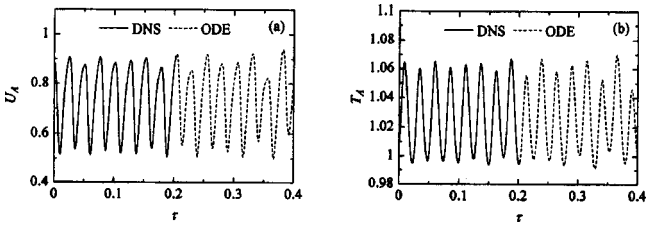

FIG. 10. Comparison between DNS results (solid lines) and low-order model results (dashed lines) at the design conditions, i.e., $Gr^0=50\,000$ and $Pr^0=0.015$. The comparison concerns the time evolution of the X-velocity (a) and the temperature (b) at the monitoring point A. For τ between 0 and 0.2, the two curves are indistinct.

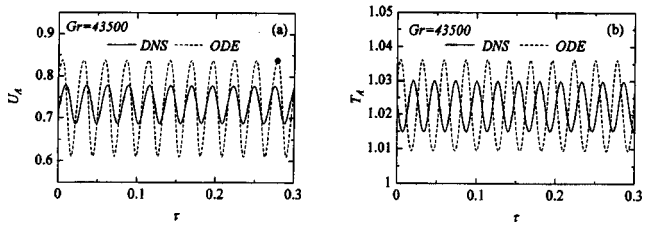

FIG. 11. Comparison between DNS results with S_L and S_A symmetries and low-order model results with the same symmetries for $Gr=43\,500$. The comparison concerns the time evolution of the *X*-velocity (a) and the temperature (b) at the monitoring point *A*. The low-order model is constructed at $Gr^0=50\,000$ from the sample shown in Fig. 4.

havior is quite well predicted by the low-order model. The oscillatory character is obtained and the frequencies are predicted within 4% of error. Only the amplitudes obtained are larger than for DNS. The predicted flow field in the P_H plane, shown in Fig. 12, is also quite similar to the DNS results [Fig. 3(b)] with the same global behavior and the same S_L and S_A symmetries.

F. Low-order model: Predicted results with only S_C symmetry

For $Gr=43\,500$, the low-order model also gives another solution which compares well with the DNS solution with only S_C symmetry. Figure 13 shows the time evolution of the predicted velocity and temperature at monitoring point *A*, together with the corresponding DNS results. The DNS behavior is here also basically predicted by the low-order model: oscillatory character, accurately predicted frequencies. The amplitudes are still less well estimated with errors which could reach 100%. The predicted flow field in the P_H plane, given in Fig. 14, has to be compared with the corresponding DNS result in Fig. 3(f). Both results have the same S_C symmetry, but look quite different in this P_H plane. The more complex flow structure obtained by the low-order model can be connected to the stronger amplitudes already observed which indicate a more convective situation. We also can mention that the comparisons are done between snapshots defined to within a phase.

G. Low-order model: Bifurcation diagram

It was also interesting to see if the low-order model was able to predict the dynamical behavior of the system. We have then determined the bifurcation diagram given by the low-order model at $Pr^0=0.015$. This bifurcation diagram

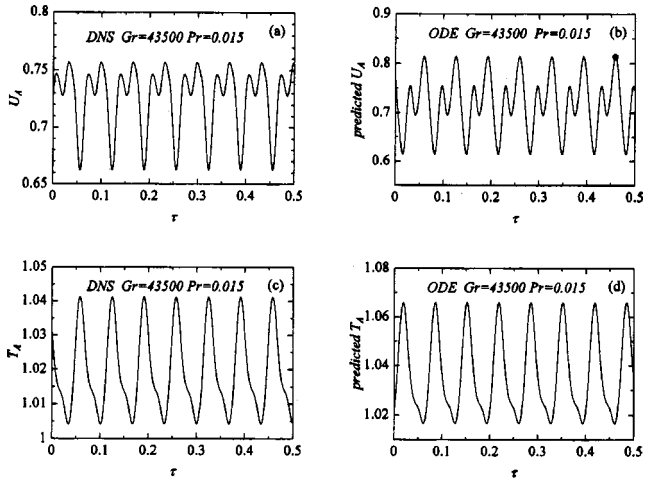

FIG. 13. Comparison between DNS results with only S_C symmetry and low-order model results with the same symmetry for $Gr=43\,500$. The comparison concerns the time evolution of the *X*-velocity (a) and (b) and the temperature (c) and (d) at the monitoring point *A*. The low-order model is constructed at $Gr^0=50\,000$ from the sample shown in Fig. 4.

calculated with the software AUTO is shown in Fig. 15 as the L^2-norm of the expansion coefficients as a function of *Gr*. Two Hopf bifurcation points (HP1 and HP2) are predicted on the steady state branch. The first Hopf bifurcation ($HP1$) occurs at $Gr_{HP1}=40\,325$ which is 6.7% lower than the DNS value ($Gr_{c1}=43\,250$) and the second Hopf bifurcation ($HP2$) occurs at $Gr_{HP2}=41\,628$. The first periodic oscillatory branch emerging supercritically at $HP1$ is stable up to $Gr=Gr_{TR}$ and unstable for $Gr>Gr_{TR}$, where Gr_{TR} is the Grashof number at which a torus bifurcation (*TR*) occurs. The second periodic oscillatory branch emerging subcritically at $HP2$ is first unstable, and then becomes stable beyond a limit point (*LP*) at $Gr=Gr_{LP}=40\,400$ which is 3.6% higher than the DNS result ($Gr_{LP,DNS}\approx 39\,000$). This periodic branch then becomes unstable at a period doubling bifurcation (*PD*) at $Gr_{PD}=55\,270$ after which a periodic oscillatory state with a twice longer period is obtained (definitions of the terms used in bifurcation analysis can be found for example in Ref. 27).

The attached velocity vectors in P_H plane (Fig. 15) are those predicted by the low-order model. The branch emerging supercritically at $HP1$ (denoted as S_L branch) corresponds to oscillatory convective states with S_L and S_A symmetries whereas the branch emerging subcritically at $HP2$ (denoted as S_C branch) corresponds to oscillatory convective states where only the S_C symmetry is kept. The predicted

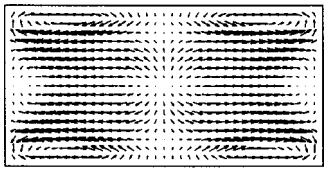

FIG. 12. View of the velocity vectors in the P_H plane for the flow with S_L and S_A symmetries predicted by the low-order model for $Gr=43\,500$. The corresponding instant is indicated by (·) in Fig. 11(a).

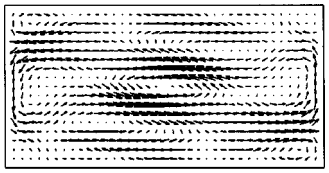

FIG. 14. View of the velocity vectors in the P_H plane for the flow with only S_C symmetry predicted by the low-order model for $Gr=43\,500$. The corresponding instant is indicated by (·) in Fig. 13(b).

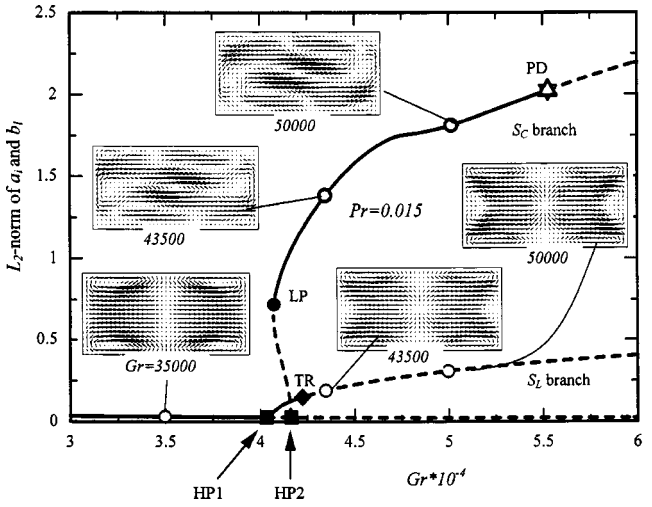

FIG. 15. Bifurcation diagram (Gr,L^2-norm of a_i and b_i) obtained from the low-order model constructed at $Gr^0=50\,000$ (L^2-norm is defined as $\sqrt{\Sigma_{i=1}^{M_V} a_i^2+\Sigma_{l=1}^{M_T} b_l^2}$). Solid lines indicate stable solutions and dashed lines unstable solutions. $HP1$: First Hopf bifurcation; $HP2$: Second Hopf bifurcation; *TR*: Torus bifurcation; *LP*: Limit point; *PD*: Period doubling bifurcation. Insets are velocity vectors in the P_H plane predicted by the low-order model for some particular values of *Gr*.

frequencies for some *Gr* values are listed in Table II together with the corresponding values obtained by DNS. In all cases, the comparisons are fairly good. Finally the results obtained by the low-order model compare rather well with the DNS results as all the important characteristics such as the critical Grashof numbers, the frequencies, the symmetries and the hysteresis phenomenon are quite well predicted.

A last information which can be obtained from the low-order model is the path of the main bifurcation points when the Prandtl number *Pr* is changed. Using the software AUTO, we have then followed the two Hopf bifurcation points $HP1$ and $HP2$ (expressed through their critical Grashof numbers) as a function of *Pr*. Figure 16 shows the stability diagram which is obtained for *Pr* varying between 0 and 0.04. It is found that Gr_{HP1} decreases monotonously with the decrease of *Pr* whereas Gr_{HP2} rather increases. When $Pr\rightarrow 0$, finite values are found for Gr_{HP1} as well as for Gr_{HP2}.

The stability diagram shows a crossing point for HP1 and HP2 branches. If we denote the value of *Pr* at the crossing point as Pr_c, then the stability diagram predicts that when $Pr<Pr_c$, with the increase of *Gr*, the flow in the cavity will first transit to an oscillatory flow with S_L symmetry and then to an oscillatory flow with S_C symmetry, and when $Pr>Pr_c$, the order of the transitions is reversed. This interesting prediction would require further verification by DNS calculations, but these calculations are still beyond our possibilities.

TABLE II. Comparison between frequencies obtained by DNS and by the low-order model constructed at $Gr^0=50\,000$ and $Pr^0=0.015$.

Branch	Gr	Frequency	
		Model	DNS
S_L	50 000	39.6	39.6
	45 000	37.5	38.7
	43 500	36.3	37.7
S_C	100 000	26.5	24.7
	50 000	16.6	16.1
	43 500	14.9	15.0

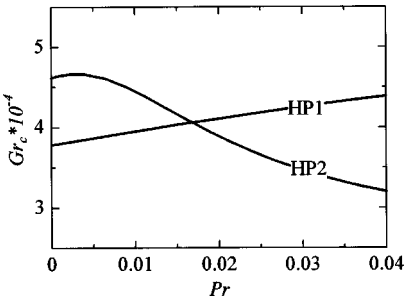

FIG. 16. Stability diagram predicted by the low-order model constructed at $Gr^0=50\,000$ and $Pr^0=0.015$. This diagram gives the variation of the critical Grashof numbers corresponding to the two Hopf bifurcations $HP1$ and $HP2$ as a function of the Prandtl number.

From the above discussions, we can conclude that the low-order model exactly reproduces the DNS results at the design conditions and qualitatively predicts the DNS results in a domain around these design conditions.

VI. DISCUSSION

A. Effect of signal length

By only changing the length of the signal which covers two, four, six or eight quasi-periods, we constructed different low-order models. Except for the model obtained from two quasi-periods, the other three models give bifurcation and stability diagrams similar to those shown in Figs. 15 and 16. Therefore, to make a reliable model from a quasi-periodic signal, this signal has to be long enough, but there is a sufficient length which is not too large. Of course, if the signal is purely periodic, one cycle is enough.

B. Effect of time interval between two successive snapshots

We collected different samples from the signal which covers about eight quasi-periods by taking snapshots at every 1000 $\Delta\tau$, 2000 $\Delta\tau$, 4000 $\Delta\tau$, and 8000 $\Delta\tau$. We then got four samples with a snapshot number of $N=408$, 204, 102, and 51, respectively. It is found that the first three models give similar bifurcation and stability diagrams as Figs. 15 and 16. Deviations are only obtained for $N=51$. Tests have also been done with smaller time intervals between snapshots as 250 $\Delta\tau$ and 500 $\Delta\tau$ for a signal covering about four quasi-periods. Results similar to Figs. 15 and 16 are still obtained. It is then found that for the accuracy of the constructed model a sufficiently small time interval between snapshots is needed, but there is no need to strongly increase the number of snapshots.

C. Effect of the number of modes

The effect of the number of modes on the behavior of the constructed low-order model has been tested. It is found that

the low-order model is sensitive to the number of modes. For the design conditions, for example, the low-order model with $M_V=4$ and $M_T=4$ gives a pure periodic solution, the model with $M_V=6$ and $M_T=4$ gives a time evolution like that obtained with $M_V=16$ and $M_T=10$. But the models with $M_V=10$ and $M_T=8$ or $M_V=22$ and $M_T=12$ give steady solutions. This inconsistency could be first caused by some lack of accuracy in the estimation of the high order less energetic POD modes and of their derivatives. These modes have stronger space and time variations and it is then more difficult to estimate them accurately. This can prevent a good convergence of the low-order model when increasing the number of modes. Moreover, in our case where velocity and temperature modes are disconnected, it seems that one must take care when pairing the number of velocity modes M_V and the number of temperature modes M_T. This could be due to the fact that for a given set of velocity modes, the temperature modes to which they are in some way connected must be included. All these conjectures will have to be confirmed in future works. As for now, the most effective way to pair M_V and M_T is to verify whether the prediction of the constructed low-order model is in good agreement with the DNS results.

D. Better choice for characteristic velocity

For the problem under consideration, there are two widely used characteristic velocities. One is $V_{\mathrm{ref}}=Gr^{0.5}\nu/h$ and another is $V'_{\mathrm{ref}}=\nu/h$. All results presented above correspond to the former choice. To show the advantages of this choice, a low-order model corresponding to the other choice of characteristic velocity was constructed and tested. The sample employed was of the same length, snapshot density and number of modes as what was used above. Note that there is no need to perform DNS again. The new sample can be obtained just by multiplying the previously used velocity by $Gr^{0.5}$. The Galerkin projection should now be applied to the following governing equations:

$$\frac{\partial \boldsymbol{V}}{\partial \tau}+\boldsymbol{V}\cdot\nabla\boldsymbol{V}=-\nabla P+\nabla^2\boldsymbol{V}+GrT\boldsymbol{e}_Z, \tag{21}$$

$$\frac{\partial T}{\partial \tau}+\boldsymbol{V}\cdot\nabla T=Pr^{-1}\nabla^2 T. \tag{22}$$

It is found that the new low-order model gives identical results at design conditions, but the results obtained when changing the Grashof number are very different. The disagreement is attributed to the lack of modification of the velocity average value (appearing in the coefficients shown in the Appendix) when the Grashof number is changed. The basisfunctions found at the design conditions form an orthogonal and complete set which is expected to be relevant for cases other than the design case. Concerning the mean values, they are expected to change when the Grashof number is modified and the low-order model should take this into account. According to Smutek *et al.*,[28] the dimensional mean values in our problem are approximately proportional to $Gr^{0.5}$ (convective situations with inertial effects). In fact the low-order models are based on constant mean values for the nondimensional velocity. This indicates that if $V_{\mathrm{ref}}=Gr^{0.5}\nu/h$ is used, the mean values of dimensional velocity are effectively proportional to $Gr^{0.5}$, whereas if $V'_{\mathrm{ref}}=\nu/h$ is used, these mean values are still constant. Therefore, for our problem, the choice of $V_{\mathrm{ref}}=Gr^{0.5}\nu/h$ as characteristic velocity greatly improves the validity of the low-order model even without correcting the mean values as was done for example in Ref. 4.

E. Advantages of independently expanding velocity and temperature

In this study, we have chosen to define two correlations matrices (6) and (7) leading to two sets of eigenfunctions (11) and (12) and then to independently expand velocity and temperature [(14) and (15) which lead to Eqs. (19) and (20)]. This procedure is different from what is suggested and used by Sirovich[3,10] and other researchers.[14,15] They define a single correlation matrix (13) leading to a single global eigenfunction and then expand the velocity and temperature by using the same coefficients $a_i(\tau)$ as

$$\boldsymbol{v}'(\boldsymbol{x},\tau)=\sum_{i=1}^{M} a_i(\tau)\boldsymbol{\Phi}_i(\boldsymbol{x}), \tag{23}$$

$$T'(\boldsymbol{x},\tau)=\sum_{i=1}^{M} a_i(\tau)\Theta_i(\boldsymbol{x}). \tag{24}$$

This second approach depends in fact on α, a constant related to the relative weighting of velocity and temperature, but also on the characteristic values chosen to nondimensionalize velocity and temperature. Different choices of α and of these characteristic values give different correlation matrices, which leads to different eigenvalues and eigenfunctions. The independent construction of two correlation matrices as is done in Eqs. (6) and (7) can avoid this indetermination.

Moreover, the use of Eqs. (23) and (24) means that the velocity and temperature fields have a same dynamical behavior. In fact, this is not always the case, especially in low-Prandtl number fluid flow (melt flows in crystal growth systems) where velocity fields usually vary more rapidly than temperature fields. The main reason for the choice we have done is that the approach corresponding to Eqs. (23) and (24) results in an incorrect stability diagram (different from Fig. 16), even though it predicts a bifurcation diagram similar to Fig. 15. In fact, this approach predicts that the critical Grashof numbers Gr_{HP1} and Gr_{HP2} increase with the decrease of the Prandtl number and go to infinity when $Pr\rightarrow 0$, a tendency which is not right according to previous two-dimensional results found in the literature.[29] By independently expanding velocity and temperature [Eqs. (14) and (15)], a more correct tendency with finite values for $Pr\rightarrow 0$ is obtained (Fig. 16).

VII. CONCLUSIONS

Proper orthogonal decomposition and Galerkin projection were employed to construct a low-order model (set of ordinary differential equations) for low Prandtl number fluid flow in a laterally heated cavity. The reliability of the constructed low-order model was examined by comparison with the results of direct numerical simulation (DNS). It is found

that the low-order model can exactly reproduce the DNS results at design conditions and fairly well approach the DNS results in a domain around these conditions. Nevertheless, one must be careful when using these low-order models, as they are very sensitive to several factors. These factors are: the length of the signal, the snapshot density, the number of modes chosen for Galerkin projection, the characteristic velocity, and the way the expansions for velocity and temperature are done. Specifically, for thermal convection in low-Pr number fluid, it is found that it is better to separate temperature and velocity when performing POD and then the Galerkin projection. At last, it seems that even a well-constructed low-order model can only be used to qualitatively predict the DNS results (such as bifurcation and stability diagrams) in a not very large range around the design conditions.

APPENDIX: COEFFICIENTS INVOLVED IN THE LOW-DIMENSIONAL DYNAMICAL SYSTEM [EQS. (19) AND (20)]

$$A_{i,j,k}=(\mathbf{\Phi}_i,(\mathbf{\Phi}_j.\nabla)\mathbf{\Phi}_k),$$

$$B_{i,j}=(\mathbf{\Phi}_i,(\overline{\boldsymbol{V}}.\nabla)\mathbf{\Phi}_j+(\mathbf{\Phi}_j.\nabla)\overline{\boldsymbol{V}}),$$

$$C_{i,l}=(\Phi_i^w,\Theta_l),$$

$$D_i=(\mathbf{\Phi}_i,(\overline{\boldsymbol{V}}.\nabla)\overline{\boldsymbol{V}}),$$

$$E_{i,j}=(\mathbf{\Phi}_i,\nabla^2\mathbf{\Phi}_j),$$

$$F_i=(\mathbf{\Phi}_i,\nabla^2\overline{\boldsymbol{V}}),$$

$$G_{l,j,m}=(\Theta_l,(\mathbf{\Phi}_j.\nabla)\Theta_m),$$

$$H_{l,m}=(\Theta_l,(\overline{\boldsymbol{V}}.\nabla)\Theta_m),$$

$$I_{l,j}=(\Theta_l,(\mathbf{\Phi}_j.\nabla)\overline{T}),$$

$$J_l=(\Theta_l,(\overline{\mathbf{V}}.\nabla)\overline{T}),$$

$$K_{l,m}=(\Theta_l,\nabla^2\Theta_m),$$

$$L_l=(\Theta_l,\nabla^2\overline{T}).$$

[1] J. L. Lumley, "The structure of inhomogeneous turbulent flows," *Atmospheric Turbulence and Radio Wave Propagation*, edited by A. M. Yaglom and V. I. Tatarski (Nauka, Moscow, 1967), pp. 166–178.

[2] G. Berkooz, P. Holmes, and J. L. Lumley, "The proper orthogonal decomposition in the analysis of turbulent flows," Annu. Rev. Fluid Mech. **25**, 539 (1993).

[3] L. Sirovich, "Turbulence and the dynamics of coherent structures Part I, II, III," Q. Appl. Math. **XLV**, 561 (1987).

[4] A. E. Deane, I. G. Kevrekidis, G. E. Karniadakis, and S. A. Orszag, "Low-dimensional models for complex geometry flows: Application to grooved channels and circular cylinders," Phys. Fluids A **3**, 2337 (1991).

[5] W. Cazemier, R. W. C. P. Verstappen, and A. E. P. Veldman, "DNS of turbulent flow in a driven cavity and their analysis using proper orthogonal decomposition," 74th Fluid Dynamics Symposium on "Application of direct and large eddy simulation to transition and turbulence," held at Chania, Crete, Greece, April 1994.

[6] R. A. Sahan, H. Gunes, and A. Liakopoulos, "A modeling approach to transitional channel flow," Comput. Fluids **27**, 121 (1998).

[7] W. Cazemier, R. W. C. P. Verstappen, and A. E. P. Veldman, "Proper orthogonal decomposition and low-dimensional models for driven cavity flows," Phys. Fluids **10**, 1685 (1998).

[8] H. M. Park and M. W. Lee, "Boundary control of the Navier–Stokes equation by empirical reduction of modes," Comput. Methods Appl. Mech. Eng. **188**, 165 (2000).

[9] H. M. Park and D. H. Cho, "Low dimensional modeling of flow reactors," Int. J. Heat Mass Transfer **39**, 3311 (1996).

[10] L. Sirovich and H. Park, "Turbulent thermal convection in a finite domain: Part I. Theory," Phys. Fluids A **2**, 1649 (1990); H. Park and L. Sirovich, "Turbulent thermal convection in a finite domain: Part II. Numerical results," *ibid.* **2**, 1659 (1990).

[11] H. Gunes, A. Liakopoulos, and R. A. Sahan, "Low-dimensional description of oscillatory thermal convection: The small Prandtl number limit," Theor. Comput. Fluid Dyn. **9**, 1 (1997).

[12] R. A. Sahan, A. Liakopoulos, and H. Gunes, "Reduced dynamical models of nonisothermal transitional grooved-channel flow," Phys. Fluids **9**, 551 (1997).

[13] H. Gunes, "Low-order dynamical models of thermal convection in high-aspect ratio enclosures," Fluid Dyn. Res. **30**, 1 (2002).

[14] B. Podvin and P. Le Quéré, "Low-order models for the flow in a differentially heated cavity," Phys. Fluids **13**, 3204 (2001).

[15] J. L. Lumley and A. Poje, "Low-dimensional models for flows with density fluctuations," Phys. Fluids **9**, 2023 (1997).

[16] "Numerical simulation of oscillatory convection in low-Pr fluids," *Notes on Numerical Fluid Mechanics*, Vol. 27, edited by B. Roux (Vieweg, Braunschweig, 1990).

[17] J. P. Pulicani, E. Crespo del Arco, A. Randriamampianina, P. Bontoux, and R. Peyret, "Spectral simulations of oscillatory convection at low Prandtl number," Int. J. Numer. Methods Fluids **10**, 481 (1990).

[18] D. Henry and M. Buffat, "Two- and three-dimensional numerical simulations of the transition to oscillatory convection in low-Prandtl-number fluids," J. Fluid Mech. **374**, 145 (1998).

[19] A. Juel, T. Mullin, H. Ben Hadid, and D. Henry, "Three-dimensional free convection in molten gallium," J. Fluid Mech. **436**, 267 (2001).

[20] M. G. Braunsfurth and T. Mullin, "An experimental study of oscillatory convection in liquid gallium," J. Fluid Mech. **327**, 199 (1996).

[21] C. J. Jing, N. Imaishi, S. Yasuhiro, and Y. Miyazawa, "Three-dimensional numerical simulation of spoke pattern in oxide melt," J. Cryst. Growth **200**, 204 (1999).

[22] T. Suzuki and H. Kawamura, "Consistency of finite-difference scheme in direct numerical simulation of turbulence," Trans. Jpn. Soc. Mech. Eng. (in Japanese) **60**, 58 (1994).

[23] C. W. Hirt, B. D. Nichols, and N. C. Romerto, Los Alamos Science Laboratory Report, LA-5852 (1975).

[24] E. Doedel and J. Kernevez, "AUTO: Software for continuation problems in ordinary differential equations with applications," Applied Mathematics Technical Report, California Institute of Technology, 1986.

[25] P. Le Quéré, "A note on multiple and unsteady solutions in two-dimensional convection in a tall cavity," ASME J. Heat Transfer **112**, 965 (1990).

[26] Y. Lee and S. A. Korpela, "Multicellular natural convection in a vertical slot," J. Fluid Mech. **126**, 91 (1983).

[27] R. Seydel, *Practical Bifurcation and Stability Analysis* (Springer-Verlag, Berlin, 1994).

[28] C. Smutek, P. Bontoux, B. Roux, G. H. Schiroky, A. C. Hurford, F. Rosenberger, and G. de Vahl Davis, "Three-dimensional convection in horizontal cylinders: numerical solutions and comparison with experimental and analytical results," Numer. Heat Transfer **8**, 613 (1985).

[29] A. Yu. Gelfgat, P. Z. Bar-Yoseph, and A. L. Yarin, "Stability of multiple steady states of convection in laterally heated cavities," J. Fluid Mech. **388**, 315 (1999).